Nanoscale

Accepted Manuscript

This article can be cited before page numbers have been issued, to do this please use: A. Böttcher, S. S. Jester, D. Löffler, J. Seibel and M. Kappes, *Nanoscale*, 2026, DOI: 10.1039/D6NR00926C.

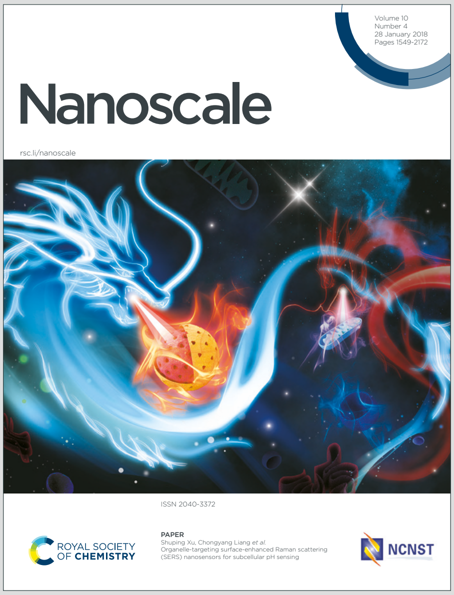

ROYAL SOCIETY
OF **CHEMISTRY**

rsc.li/nanoscale

View Article Online
DOI: 10.1039/D6NR00926C

All-Carbon Patterning of HOPG on the Nanometer Scale with non-IPR Fullerenes

Artur Böttcher[a], Stefan-Sven Jester[b], Daniel Löffler[a], Johannes Seibel[a] and Manfred M. Kappes[a,c*]

[a]Institute of Physical Chemistry, Karlsruhe Institute of Technology, Kaiserstraße 12, 76131 Karlsruhe, Germany;

[b]Kekulé-Institut für Organische Chemie und Biochemie, Rheinische Friedrich-Wilhelms-Universität Bonn, Gerhard-Domagk-Str. 1, 53121 Bonn, Germany;

[c]Institute of Nanotechnology, Karlsruhe Institute of Technology, Kaiserstraße 12, 76131 Karlsruhe, Germany.

Abstract

Arrays of amorphous carbon defects were prepared on the basal plane of highly oriented pyrolytic graphite (HOPG) using Ga^+ focused ion beam (FIB) writing. These defects were then used as pinning sites for non-IPR C_{58} fullerene cages (with reactive adjacent pentagon rings) deposited onto the room temperature surface from a low-energy (< 6 eV) mass-selected ion beam. Following deposition, a brief annealing step at 550 K increased the occupation of the FIB defects by allowing for pinning of additional C_{58} cages diffusing from more weakly binding sites elsewhere on the surface. The overall pinning efficiency depends on the lattice constant of the FIB defect array. When the defect spacing approaches the mean gliding length of mobile C_{58} cages (reflecting surface parallel velocity dissipation following hyperthermal impact on the superlubric HOPG) nearly complete decoration of the FIB defects can be achieved. Upon further heating to 1100 K, a significant fraction of the pinned C_{58} can be transformed into non-volatile polymers of partially fused cages. Alternatively, heating the C_{58} island arrays while exposing them to atomic hydrogen can largely remove the FIB-structured deposits by converting them into volatile fullerene hydrides. The results demonstrate a tunable, carbon-on-carbon patterning strategy with potential for nanodevice fabrication.

Keywords

All-carbon patterning, Focused ion beam (FIB) nanostructuring, Non-IPR fullerenes, Soft-landing ion beam deposition, Graphite/HOPG surface modification, carbon nanostructures.

*Corresponding author: Manfred Kappes, Institute of Physical Chemistry, KIT
E-mail address: manfred.kappes@kit.edu

View Article Online
DOI: 10.1039/D6NR00926C

1. Introduction

Carbon- and in particular graphene-based nanoelectronics continues to attract attention for its potential to yield high-speed, low-power, and quantum-coherent devices.[1] Achieving the next level of performance will require more precise control of structure and composition at the nanometer scale, including the ability to locally tune the electronic or (nuclear) spin environment. In this context, nanoscale regions of "amorphous"[2] and/or isotopically-enriched-carbon[3] embedded in an otherwise crystalline ^{12}C matrix are particularly attractive goals. Controllably structuring such regions with atomic precision could enable local band-gap engineering, improved thermal management, or even spin-qubit architectures based on controlled hyperfine coupling. Among the techniques for graphene patterning,[4] Focused Electron Beam Induced Deposition (FEBID) provides a bottom-up additive route with nanometer precision, though the resulting deposits often struggle with organic contamination and low sp^2 content.[5] Conversely, Helium Ion Beam Milling (HIBM) offers a high-resolution subtractive method that minimizes structural damage relative to traditional ion beams, albeit at the cost of scalability.[6] For high-throughput applications, Laser-Induced Graphene (LIG) enables the photothermal conversion of precursors into porous graphitic networks, though its resolution remains restricted to the micrometer regime.[7]

Focused Ion Beam (FIB) nanostructuring offers a powerful top-down route to realize such functional architectures at the nanometer scale. Commercial Ga^+ and He^+ FIB systems typically use incident ion kinetic energies between 10 – 35 keV and can achieve 5 – 30 nm beam diameters at surfaces with nanometer targeting accuracy. For bulk scale targets, however, secondary processes such as collisional cascading, atom backscattering, sputtering and redeposition can significantly broaden the surface area affected by ion impact limiting structuring resolution to > 50 nm – depending in detail on the material. FIB nanostructuring can be applied to the full range of carbon-based materials including single- or few-layer graphene.[8] While thinner targets reduce secondary broadening effects, FIB processing of supported graphene becomes particularly sensitive to background contamination.[9] To enable precise and reproducible modification of graphene-type materials, new ultrahigh-vacuum (UHV)-compatible approaches relying on all-carbon (additive) molecular building blocks need to be developed.

The use of fast ion beams to nanostructure graphite surfaces has a long history. Bräuchle et al. employed energetic C_{60}^+ implantation followed by controlled oxygen etching to produce nanometer-scale pits of controllable depth in highly oriented pyrolytic graphite (HOPG), demonstrating one of the first examples of directed carbon removal at the nanoscale.[10,11] Subsequently, Beebe et al. used Ga^+ FIB to generate periodic arrays of such etch pits and to show that they could be used as templates for the thermal deposition of gold atoms.[12] Melinon and co-workers extended this concept to Ga^+ FIB written periodic lattices of amorphous carbon defects also demonstrating for the first time *defect mediated trapping* of a size-distribution of 500 -100 atomic neutral gold- and (later) cobalt-platinum clusters perpendicularly incident from a supersonic molecular beam at nominal kinetic energies, E_{kin}, of ca. 1 keV per particle.[13,14]

View Article Online
DOI: 10.1039/D6NR00926C

Over the following years, the Karlsruhe group systematically developed FIB-based nanostructuring of HOPG [15] and showed, e.g., that Ga^+ FIB structured patterns of amorphous carbon could be selectively etched to yield stacked nanographene blocks.[16] These so-called etch-assisted FIB (EFIB) techniques achieved lateral control in the 100 nm × 100 nm range and established the use of amorphous carbon as a reactive intermediate for shaping graphite. More recently, Böttcher et al. demonstrated similar patterning of single layer graphene on SiO_2/Si substrates using He^+ FIB, producing arrays of well-defined ca. 70 nm diameter $Si_xO_yC_z$ defects suitable for subsequent cluster deposition and catalytic studies.[17]

Parallel to these developments, several of the authors have also extensively applied “soft-landing” ($E_{kin} < 6eV$) ion beam deposition, to probe the mobility and on-surface reactions of fullerene-based, all-carbon cages on HOPG. In particular, low kinetic energy deposition of cages with reactive annelated pentagon rings, e.g. (non-IPR) C_{58}, was demonstrated to form covalently linked aggregates with significantly stronger cohesion and different electronic properties than similarly prepared islands of (IPR) C_{60} (comprising the well-known icosahedral cage with unreactive **I**solated **P**entagon **R**ing structure).[18] Jester et al. used ex-situ AFM to show that low-energy deposition of non-IPR fullerene cations is associated with four general steps following neutralization: (i) conversion of normal impact energy into hyperthermal, surface-parallel “gliding” motion; (ii) frictional energy dissipation over a mean free path of several hundred nanometers; (iii) (equilibrium) thermal surface diffusion and finally (iv) immobilization.[19] Specifically, C_{58} deposited onto HOPG was observed to exhibit long-range lateral mobility over hundreds of nanometers before becoming immobilized at reactive defects such as step edges, which act as capture and nucleation sites. Hence, following the metal cluster-trapping concept established by Mélinon and co-workers [13,14,20], which relied on keV-scale incident energy and polydispersed metal clusters, while this study uses 6 eV soft-landing and monodispersed C_{58} cages and deliberately introduced defect arrays (e.g. by FIB) to enable controlled C_{58} cage capture and island growth.

The present study shows that FIB defect arrays can indeed enable precise and reproducible nanometer scale all-carbon (additive) modification of graphitic materials under UHV. Specifically, we demonstrate that Ga^+ FIB-written amorphous carbon defects in HOPG can serve as precise pinning sites for C_{58}-derived aggregates/islands ($(C_{58})_n$) formed upon soft-landing of mass-selected non-IPR fullerene ions (C_{58}^+). The soft-landing approach combines control of the mass-to-charge ratio (and kinetic energy) of the projectile species with the clean surface environment required for reproducible chemical functionalization, going beyond earlier metal cluster deposition studies that relied on deposition of wide size distributions of much larger particles at significantly higher incident kinetic energies.[13,14,20] Our study unites two previously distinct capabilities — precise nanostructuring by focused ion beams and molecularly defined non-IPR fullerene deposition — to realize a new, controllable, all carbon route to additive nanoscale patterning of graphitic materials.

View Article Online
DOI: 10.1039/D6NR00926C

2. Experimental Section

Freshly cleaved SPI HOPG grade 2 substrates were patterned by Ga^+ FIB (Zeiss EsB 1540, 30 keV, 10 pA, 0.4 ms dwell time per spot) to create five different periodic square lattice arrays of amorphous carbon hillocks with lattice constants a = 300, 450, 600, 750 and 900 nm. The morphology of individual FIB defect structures (shape, height, diameter) depends strongly on the Ga^+ ion dose used. Substrates patterned with a dose dose of $D = 2.5 \times 10^4$ ions/spot were found to be most suitable for studying the templated growth of C_{58} islands – and were used throughout. Fig. S1 and Fig. S2 in Supporting Information illustrate the morphology dependence on the Ga^+ ion dose of the FIB arrays in more detail, including AFM and STM images acquired under ambient conditions. Raman spectra of defect regions obtained under comparable conditions show a high ratio of D- to G-line intensity (I_D/I_G~ 0.5)[16] indicating that such hillocks consist predominantly of amorphous carbon with a significant fraction of sp^3 bonding.

These FIB patterned samples were then transferred into an ultrahigh-vacuum (UHV) system (base pressure $< 1 \times 10^{-9}$ mbar) equipped with facilities for low-energy ion-beam deposition (LEIBD), X-ray and ultraviolet photoelectron spectroscopy (XPS, UPS), and mass-resolved thermal desorption spectroscopy (TDS). Prior to fullerene ion deposition (onto substrates held at room temperature), the patterned HOPG sample was cleaned by flash heating it three times up to 1400 K (in-situ). In this way surface adsorbates (e.g. water) and intercalated molecules (e.g. O_2) could be removed - resulting in cleaned terraces, uncovered defect regions as well as undercoordinated C-atoms at armchair or zig-zag step edges.[21]

Non-IPR C_{58}^+ ions were generated by electron-impact fragmentation/ionization of C_{60} vapor in a dedicated ion source and mass-selected with a quadrupole mass filter using a low-energy ion beam deposition (LEIBD) system which has been described previously.[18] The resulting C_{58}^+ ions were electrostatically steered through several differential pumping stages and softly landed on FIB-patterned HOPG under UHV. For this study we chose an incident kinetic energy of 6 ± 0.5 eV (set by applying a retarding field to the sample), low enough to preserve cage integrity upon impact but sufficient to induce an initially large amount of surface parallel motion. The deposited C_{58}^+ flux was typically 3×10^{11} ions/cm^{2}s, and coverages achieved were typically 0.3 – 1 monolayer (ML) as monitored by the total deposition time and beam current equivalent. These parameters were calibrated by combining TPD and AFM imaging to determine the ionic dose required to reach a saturated monolayer of C_{60}/HOPG.

After deposition, the as-prepared samples were either directly analyzed at room temperature or annealed in UHV at 550 K for 10 min to promote surface diffusion and island coalescence before further characterization by ex-situ AFM and/or STM. In some cases, we also flashed C_{58} decorated samples to 1100 K and measured the flux of desorbing C_{58} cages. In several measurements, C_{58} deposits were reacted with an effusive flux of 2.7×10^{14} D/cm^{2}s of atomic

View Article Online
DOI: 10.1039/D6NR00926C

deuterium generated in a microwave plasma source operating at p(D_2) = 4 × 10^{-5} mbar (Tectra, Plasma Source GenVII).

Ex-situ AFM imaging (Veeco CP2) was performed under ambient conditions using a silicon cantilever with nominal tip radius < 10 nm. Topographic data were processed using standard plane subtraction and flattening routines with Gwyddion.[22] Ex-situ STM imaging (Veeco CP2, STM mode) under ambient conditions was carried out using freshly cut PtIr tips and conditions as indicated.

3. Results and Discussion

3.1 Morphology of FIB-Patterned Defects. AFM imaging confirmed that Ga^+ FIB irradiation under the conditions used produces ordered arrays of amorphous hillocks embedded in atomically flat terraces (Figure 1a). Each defect feature exhibited a mean diameter of ~100 nm and a height of 2–3 nm, depending in detail on the ion dose, which is in agreement with Ga^+ FIB spot formation described in literature.[14] Their square lattice arrangement remained uniform across micron-scale regions as indicated in Figure 1. This procedure provides spatially well-defined amorphous carbon defect sites, which we have previously shown can be readily thermally etched by O_2 (to form CO and CO_2), suggesting that they are rich in both under-coordinated and also sp^3 C atoms. This makes them much more reactive than neighbouring pristine graphite (basal plane) regions.[15] We will demonstrate below that these amorphous carbon defects are also suitable for capturing reactive non-IPR fullerenes moving across the surface, similar to the controlled capture of large metal clusters described earlier.[20] For more details of the morphology of the FIB defects see Fig. S1 and Fig. S2 in Supplementary Data.

3.2 Growth of C_{58} films on pristine HOPG. Before studying patterned surfaces, we revisit the initial stages of island growth upon “soft-landing” of C_{58} on pristine HOPG at room temperature – as outlined in reference [19]. During soft landing, the C_{58}^+ projectiles rapidly neutralize on the conductive HOPG, so that the subsequent diffusion, pinning and inter-cage reactions involve neutral C_{58} (and C_{58}-derived aggregates). We use “C_{58}-derived” to denote deposits that originate from soft-landed molecular C_{58} and may include covalently linked oligomers/polymers in addition to intact, unaltered cages. The resulting surface mobility of C_{58} and aggregation are governed by how the initially hyperthermal impact energy is dissipated on HOPG. This is associated with efficient conversion of hyperthermal incident kinetic energy into fast surface-parallel gliding motion (primarily via coupling of rotational/vibrational excitation of the projectiles with substrate deformation during impact) which must be dissipated before thermalization can occur. At E_0 = 6 eV, the impact energy used in this study, the gliding length before thermalization was found to be surprisingly long: $\Lambda \approx 300$ nm and comparable to the typical terrace width of high-quality HOPG (which can be rationalized in terms of quantum-limited friction of the fullerene cage moving on the near-superlubric HOPG surface).[19,23] Here, Λ denotes the mean hyperthermal gliding length prior

View Article Online
DOI: 10.1039/D6NR00926C

to thermalization; subsequent redistribution is governed by conventional thermal surface diffusion. This gives rise to preferential nucleation of two-dimensional dendritic island growth at step edges or domain boundaries. For large enough terrace regions, additional nucleation of islands is observed "on-terrace" (e.g. at missing carbon atoms), suggesting that some surface-diffusion limited aggregation can also occur following the gliding stage. Figure 2 shows a typical set of AFM images – before and after decoration of pristine HOPG with C_{58}. Note the selective decoration of step edges as well as formation of fractal islands on wide

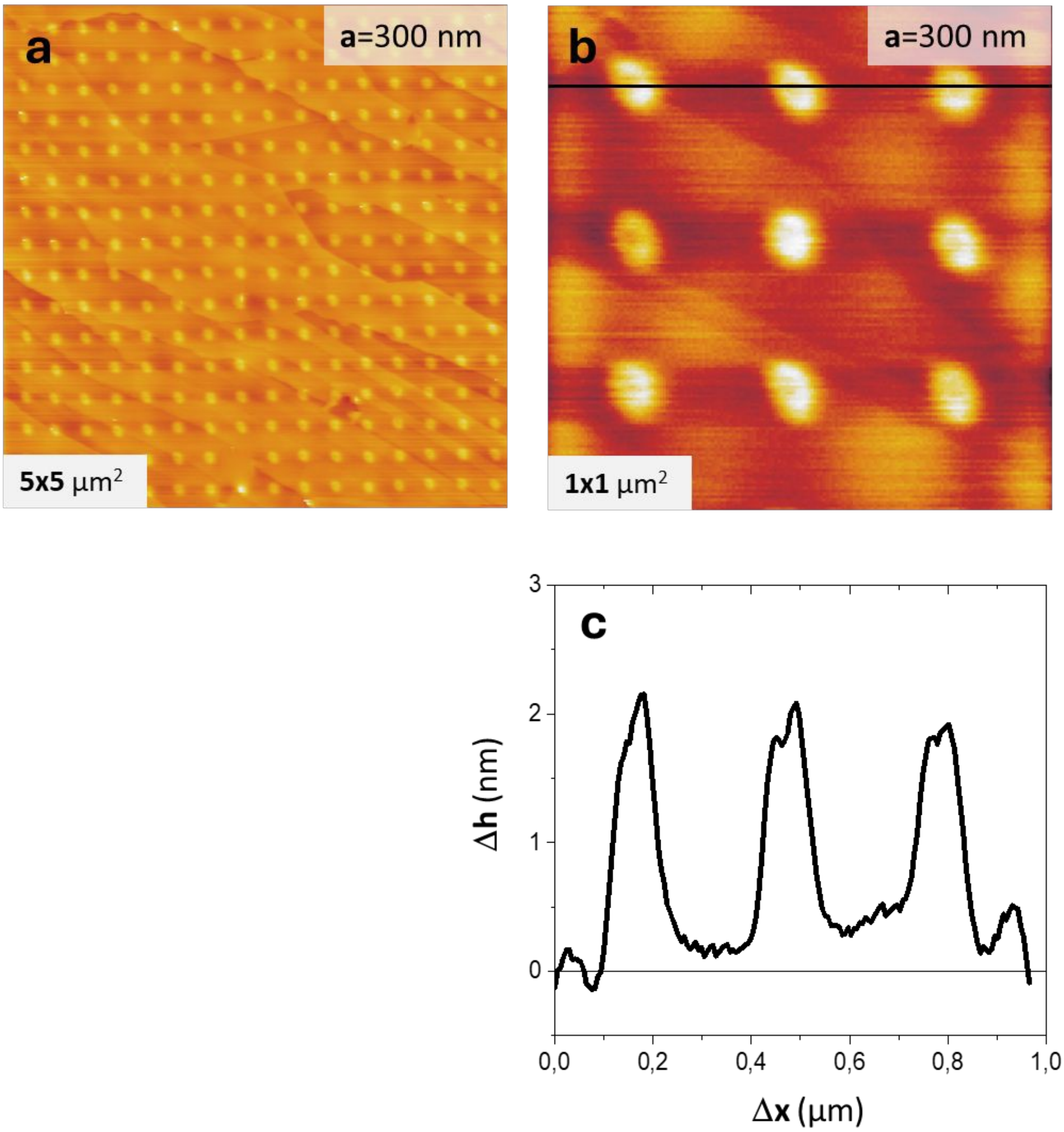

Fig. 1 (**a**, **b**) AFM images at two different magnifications (**a**: 5 × 5 μm², **b**: 1 × 1 μm²) and a cross-sectional height scan of a typical array (from **b**, as indicated) of amorphous carbon defects generated by Ga^+-FIB patterning of HOPG with a lattice constant of $a \approx 300$ nm. Bright spots correspond to hillocks (mean height 2-3 nm, mean feature size ~100nm). The array of amorphized spots overlaps with randomly distributed step edges (mean height <0.5 nm; <10 steps/μm²). Patterning conditions: Ga^+ ion current I = 10 pA, exposition time per spot t = 0.4 ms, dose D = 2.5 × 10^4 ions/spot.

View Article Online
DOI: 10.1039/D6NR00926C

terraces. The relationship between typical terrace width and gliding length Λ defines the length scale for optimal FIB patterning as we will see next.

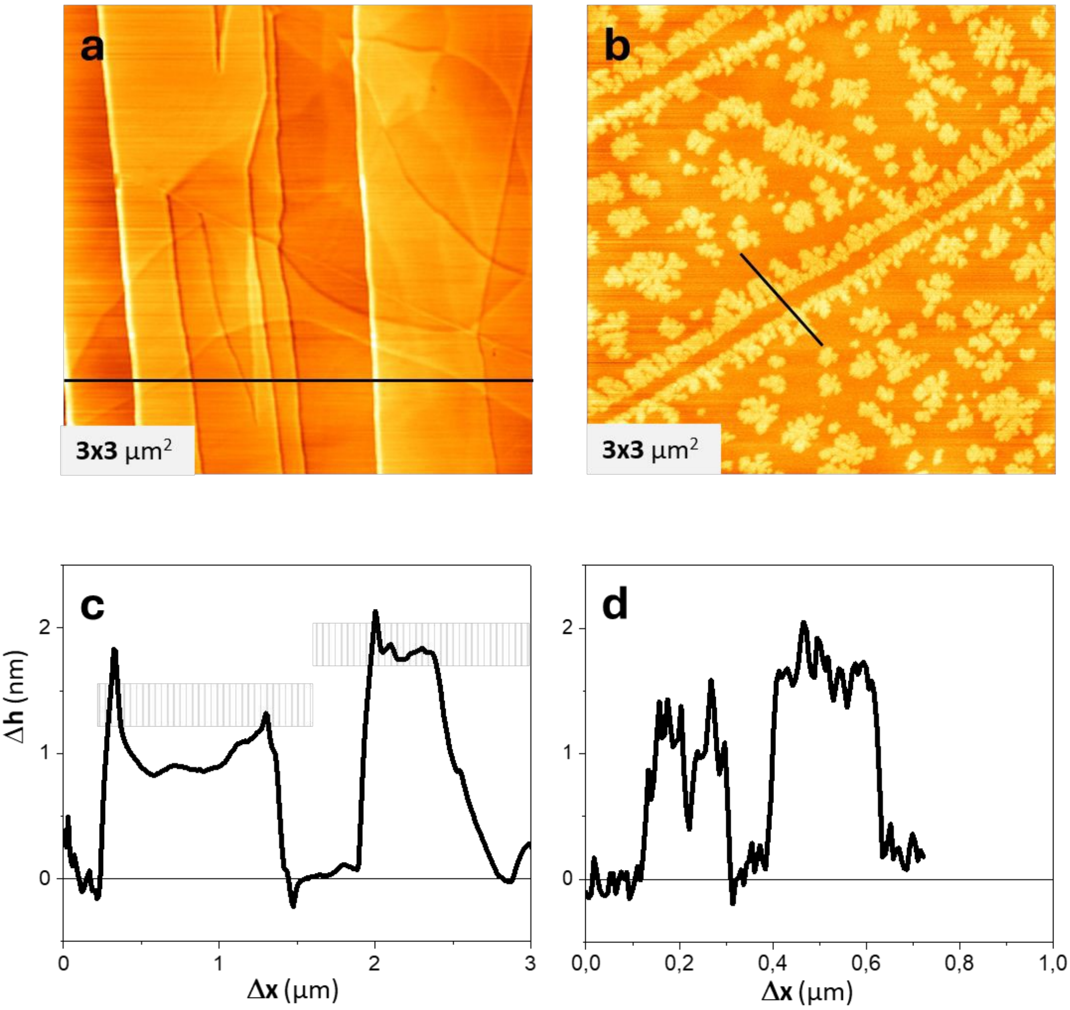

Fig. 2: AFM images (3 × 3 μm^2) and corresponding line scans (below) showing: (**a**) a freshly cleaved pristine HOPG surface and (**b**) the HOPG surface after soft-landing deposition of C_{58}^+ ions (E_0 = 6 eV; Θ = 1 ML corresponding to a nominal coverage of 10^6 cages/μm^2). Note that in the initial stages of deposition C_{58} cages stick predominantly to step edges (acting as "natural" reaction centers). After the 1 ML exposure shown we observe: (i) a high lateral density of large 2D dendritic C_{58}-derived islands on wide terrace regions, consistent with aggregation/oligomerization of reactive non-IPR cages (including covalent linking), and (ii) a lower lateral density of small islands on narrow terraces.

3.3 Controlled Decoration of FIB Arrays. When 1 ML of C_{58}^+ ions was deposited onto FIB-patterned substrates and subsequently thermally annealed in-situ for ten minutes at 550 K, ordered arrays of islands were formed preferentially at the defect sites (Figure 3). AFM images and line profiles (see Fig. S2) indicate that the resulting C_{58}-derived islands have mean heights comparable to those of the amorphized spots (≈ 2 nm). This suggests that island growth takes place preferentially by attachment of mobile cages to the *rims* of amorphous carbon regions (with the occasional exception of “on-top” sticking decoration by directly incident C_{58}^+ cages).

For a FIB lattice constant of *a* = 300 nm (≈ Λ), this procedure led to nearly every amorphous carbon spot being decorated by an C_{58}-derived island, while the surrounding terrace regions remained comparatively clean. To quantify this, we define an island coverage, $\Theta_{i/s}$, as the fraction (ranging between 0 and 1) of the surface covered by islands of two distinguishable types, “on-terrace” (Θ_i) and “FIB defect-pinned” (Θ⍰). For uniform doses of 1 ML of C_{58}^+ ions, increasing the patterning lattice constant under otherwise identical conditions progressively reduced the coverage of islands associated with FIB defects, whereas the coverage of islands decorating terrace regions increased. The degree of registry of C_{58}-derived islands with pinning sites (proportional to Θ⍰) decreases with higher lattice constant, confirming that efficient pinning occurs only when the defect spacing approaches the mean gliding length of mobile C_{58} cages at the incident energy used (Figs. 3 and S3). In this picture, the initial hyperthermal gliding sets the characteristic capture length scale (Λ), while subsequent thermal diffusion during the 550 K annealing step governs redistribution from weaker trapping sites (terrace islands and step-edge bound species) and promotes defect-site occupation.

Note that the annealing step was critical for achieving high registry. After deposition at room temperature, only partial occupation of the FIB sites was observed, with many C_{58} species (and early-stage aggregates) also trapped in islands on terraces and at step edges. Upon heating to 550 K, a large fraction of these weakly bound cages can diffuse and react at under-coordinated carbon atoms associated with the amorphous carbon defect regions. Presumably, formation of C–C bonds between the 2AP (= annelated pentagon pairs) sites of C_{58} and reactive surface C-atoms stabilizes the pinned species, while 2AP–2AP intercage bonding drives the consolidation of the islands. The overall result is a sharp increase in decoration of pinning sites and more uniform registry across large areas (Fig. S4).

It is interesting to note in passing that C_{60} soft-landed under the same conditions has an even longer gliding length on HOPG compared to C_{58} and forms large compact islands *which are predominantly not associated* with the FIB defects (see Fig. S5). IPR C_{60} is too weakly bound both to defects and to neighbouring fullerenes for the pinning process to work.

View Article Online
DOI: 10.1039/D6NR00926C

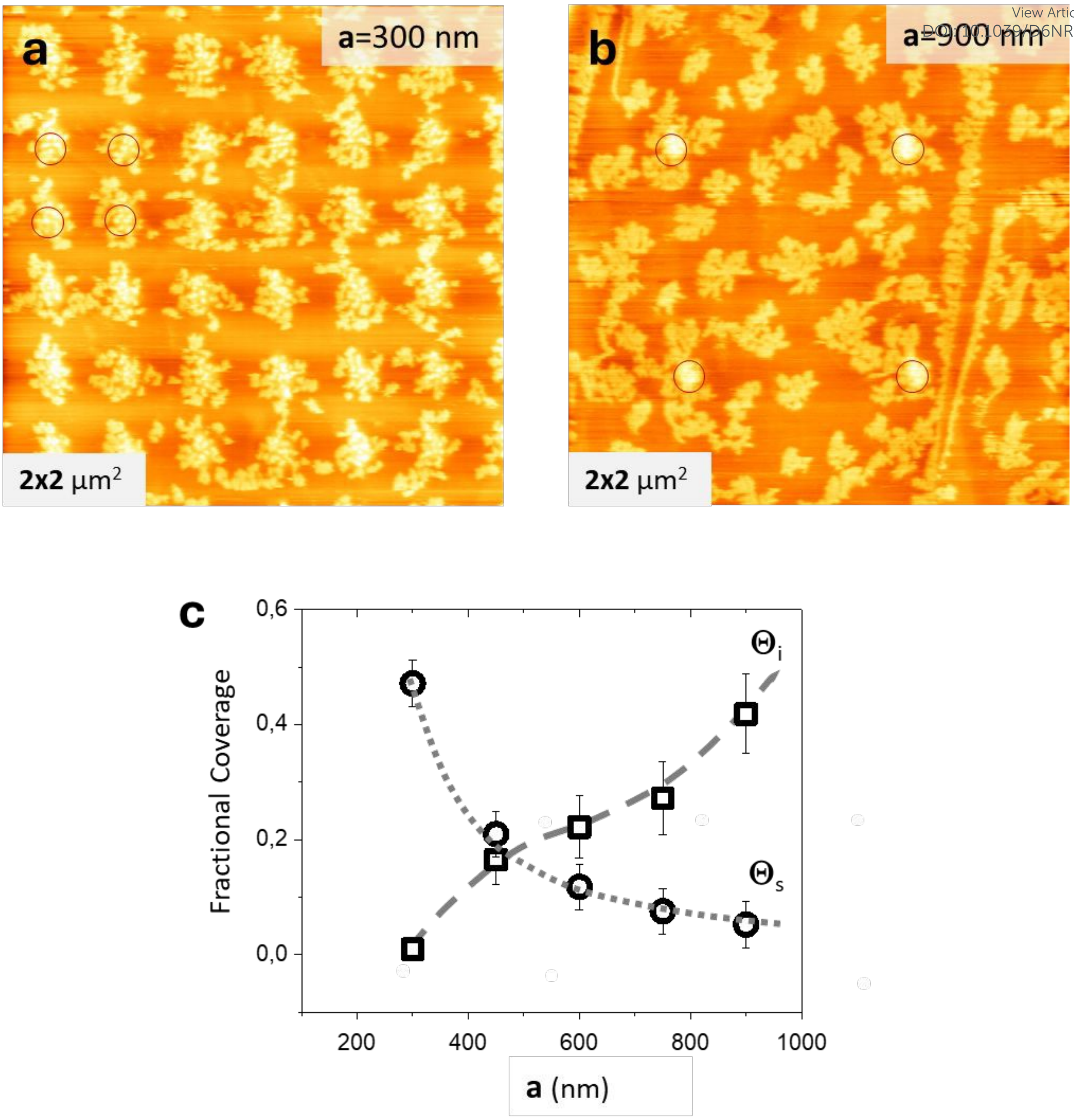

Fig. 3: AFM images (2 × 2 μm^2) after deposition of C$_{58}^{+}$ ions onto amorphous carbon arrays with different lattice constants, a, followed by annealing to 550 K for ten minutes (shown are *a* = 300 nm (**a**) and 900 nm (**b**)). (**c**) Plot of the resulting coverages (Θ) of C$_{58}$-derived islands not associated with defect sites, Θ_i, versus coverage of islands at FIB spots, Θ⍰ – as a function of the lattice constant of the amorphous carbon array (for additional AFM images see Fig. S4). Dotted lines are meant to guide the eye. The fractional coverage of islands associated with FIB spots decreases with increasing FIB patterning lattice constant (*a* = 300–900 nm). Conditions: FIB: I = 10 pA, t = 0.4 ms, $D^+ = 2.5 \times 10^4$ ions/spot; LEIBD: E_0 = 6 eV, Θ = 1 ML C$_{58}$, A [10′/550 K].

3.4 Thermal Stability and Transformation. In studies of the thermal stability *of submonolayer and continuous (multilayer)* C$_{58}$-derived films deposited on pristine HOPG under UHV (using AFM imaging, UPS and Raman spectroscopy as well as thermal desorption), we observed that heating to 1100 K leads both to cage desorption and formation of a non-desorbable

View Article Online
DOI: 10.1039/D6NR00926C

carbonaceous material. [18,24] This has significantly reduced band gap compared to the as prepared C_{58}-derived multilayer (which shows semiconducting properties). This on-surface reaction product was attributed to “cage-coalescence polymerization”.[24,25] Depending on the initial thickness of the deposited film, between 10% (for 1 ML) and 100% (for 120 ML) of the deposit can be converted to this polymeric material by flashing to 1100 K.

Consistent with this, in the present study we observed that heating C_{58}-derived island arrays pinned at defects (prepared as indicated in the previous section) to 1100 K induces pronounced morphological changes also indicative of partial desorption. Whereas the C_{58}-derived islands initially decorate the defects quite uniformly, flash heating transforms them into highly anisotropic networks of linear and branched chains radiating away from the FIB defect sites (Figure 4). The observed height of these features (0.7–0.8 nm) is on the order of the C_{58} cage diameter, consistent with the formation of fused cage polymers.

3.5 Removal of Deposits and Chemical Control. In our previous studies of C_{58}-derived thin films prepared on pristine HOPG we also showed that deuteration via exposure to a flux of near-thermal deuterium atoms weakens 2AP–2AP intercage bonds and eventually leads to the formation of individual deuterofullerene cages which have a significantly lower desorption activation energy than C_{58}. Consequently, thin films of the deuterated material can be sublimed (in contrast to the as-prepared C_{58} deposit).[25] To test the chemical stability of our prepatterned C_{58}-derived island arrays we similarly exposed them to atomic hydrogen/deuterium at 550 K. Subsequent heating to 1100 K led to essentially complete removal of the deposited fullerene material from the surface (Figure 4c), yielding a surface morphology consistent with the clean FIB-patterned template. However, we cannot exclude surface modifications induced by hydrogen/deuterium exposure and subsequent heat treatment [26,27]. Gauging the potential of our method for *reconfigurable* all-carbon patterning would therefore require further work beyond the scope of this study, e.g., atomically resolved (spectro-) microscopic imaging.

View Article Online
DOI: 10.1039/D6NR00926C

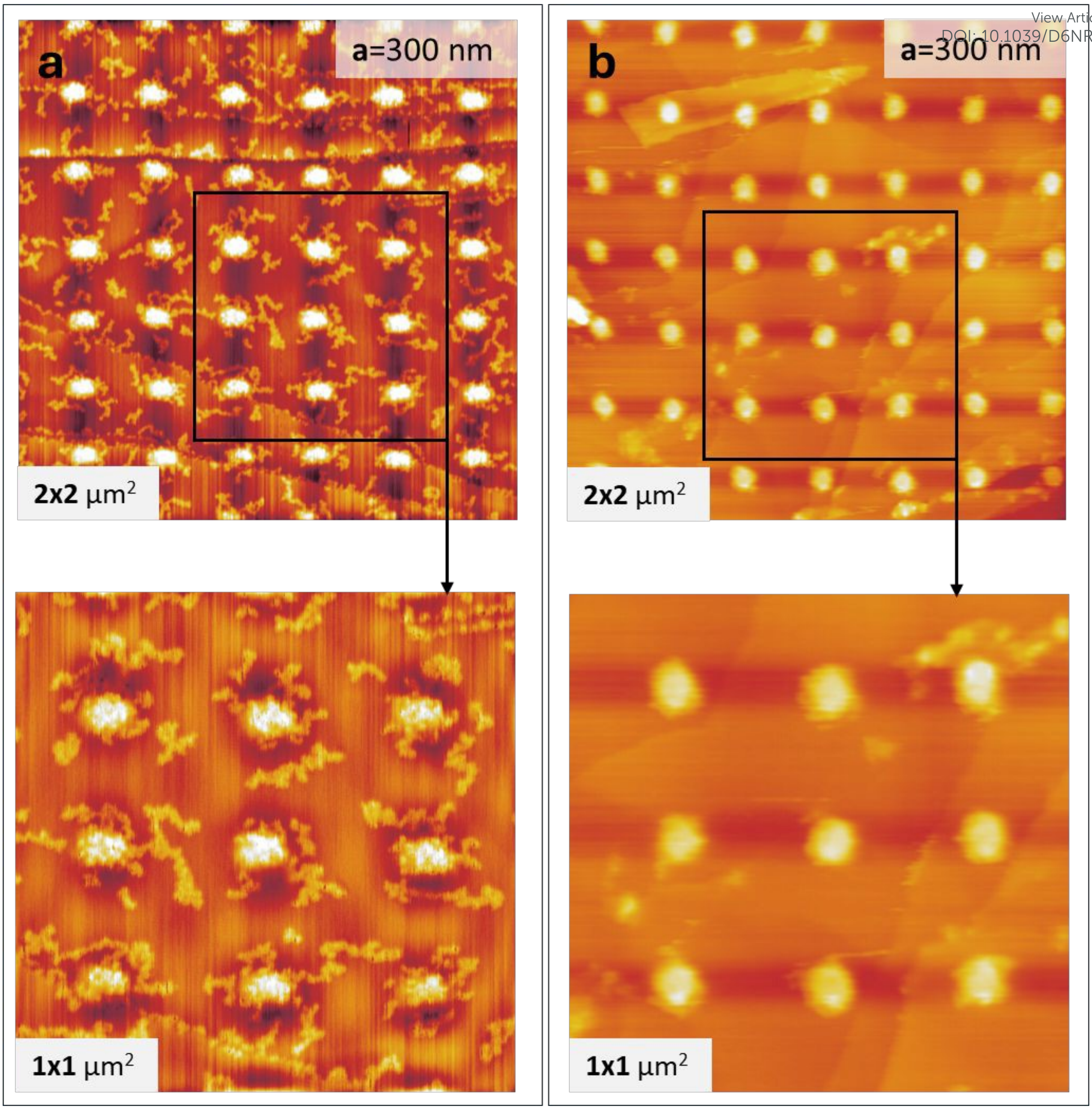

Fig. 4 AFM images (2 × 2 μm² and 1 × 1 μm²) illustrating morphological changes to C_{58}-derived islands pinned on a 300 nm lattice constant array of amorphous carbon defects (cf. Fig. 3a) as *induced by flashing to 1100K under UHV* (**a**) or after exposure to atomic hydrogen/deuterium at 550 K, followed by heating to 1100 K (**b**). (FIB/HOPG array: I = 10 pA, t = 0.4 ms, D = 2.5 × 10^4 Ions/spot, *a* = 300 nm; initial C_{58} decoration: E_0= 6 eV, Θ = 1 ML, annealing [10'/550K]). The brighter features on and adjacent to the patterned FIB defects are assigned as linear and branched chains of fused C_{58} cages.

4. Summary and Outlook

By combining Ga^+ FIB patterning with low-energy, mass-selective deposition of non-IPR fullerene ions followed by thermal annealing, we have demonstrated a tunable, UHV-compatible strategy for additively structuring molecular carbon on graphite with high lateral resolution. Specifically, we have written arrays of ca. 100 nm diameter amorphous carbon defects and selectively decorated them with C_{58}-derived islands consistent with

View Article Online
DOI: 10.1039/D6NR00926C

(predominantly) covalent intercage linking. The registry of these islands with the FIB-patterned defects (versus nucleation elsewhere on the surface) depends on: (i) the lattice constant of the defect array and its relation to the average "gliding" length of deposited cages and (ii) the extent of surface diffusion during a subsequent thermal annealing step which enhances capture of non-IPR fullerene cages at the amorphous carbon hillocks. The semiconducting C_{58} deposits can be partially transformed into fused-cage polymers by flash heating to 1100 K – resulting in networks of linear and branched chains radiating away from the FIB defect sites. Deposits can be largely removed chemically by exposure to H atoms followed by thermal desorption of $C_{58}H_x$. It remains unclear, however, whether the initial chemical state of the patterned surface is fully recovered.

This carbon-building-block-based system not only provides a cage-size tunable model platform for studying defect-mediated cluster immobilization and inter-cage reactivity (e.g. C_{58} vs. C_{60}), it also offers an all-carbon patterning strategy that may be of interest for exploring nanodevice concepts, e.g., encompassing engineering of electromagnetic contrast via local permittivity and permeability changes.[28] Potential next steps include extending the approach to smaller defect features by using low-dose He^+ FIB and (thinner) targets of free-standing ^{12}C graphene mono-/multilayers followed by soft-landing deposition of ^{13}C enriched fullerenes and photothermal annealing thereof.

CRediT authorship contribution statement

Artur Böttcher: Writing – review & editing, Writing – original draft, Visualization, Methodology, Investigation, Formal analysis. **Stefan-Sven Jester:** Investigation, Formal Analysis. **Daniel Löffler:** Investigation, Methodology. **Johannes Seibel:** Writing – review & editing. **Manfred Kappes:** Writing – review & editing, Writing – original draft, Visualization, Supervision, Resources, Methodology, Investigation, Funding acquisition, Formal analysis, Conceptualization.

Acknowledgements

We gratefully acknowledge support of this work by KIT, Land Baden-Württemberg and the German Science Foundation (DFG). We also thank Seythan Ulas and Jürgen Weippert whose multiple experimental contributions to the Karlsruhe Depo-1 effort also helped to make this paper possible. We further thank Fabián Pérez-Willard and Patrice Brenner for FIB patterning of HOPG samples and their technical support.

Declaration of competing interests

The authors have no competing interests to declare.

View Article Online
DOI: 10.1039/D6NR00926C

Appendix A. Supplementary data

Supplementary data to this article can be found online at https://doi. ……

Data availability

The data presented in this manuscript are available upon request.

References

[1] R. Kraft, M.-H. Liu, P. B. Selvasundaram, S.-C. Chen, R. Krupke, K. Richter, R. Danneau, "Anomalous Cyclotron Motion in Graphene Superlattice Cavities" *Phys. Rev. Lett.* **2020**, *125*, 217701.

[2] W. Luo, W. Cai, Y. Xiang, W. Wu, B. Shi, X. Jiang, N. Zhang, M. Ren, X. Zhang, J. Xu, "In-Plane Electrical Connectivity and Near-Field Concentration of Isolated Graphene Resonators Realized by Ion Beams" *Advanced Materials* **2017**, *29*, 1701083.

[3] V. Strenzke, M. Prada, J. M. J. Lopes, L. Tiemann, R. H. Blick, "The quest for harnessing nuclear effects in graphene-based devices" *Appl. Phys. Reviews* **2024**, *11*, 011312.

[4] S. Abrahamczyk, O. Sakreida, A. Bachmatiuk, G. S. Martynková, M. H. Rümmeli, "Developments in Nanopatterning of Graphene; Toward Direct Writing" *Advanced Materials* **2026**, *38*, e13264.

[5] I. Utke, P. Swiderek, K. Höflich, K. Madajska, J. Jurczyk, P. Martinović, I. B. Szymańska, "Coordination and organometallic precursors of group 10 and 11: Focused electron beam induced deposition of metals and insight gained from chemical vapour deposition, atomic layer deposition, and fundamental surface and gas phase studies" *Coordination Chemistry Reviews* **2022**, *458*, 213851.

[6] N. Kalhor, S. A. Boden, H. Mizuta, "Sub-10 nm patterning by focused He-ion beam milling for fabrication of downscaled graphene nano devices" *Microelectronic Engineering* **2014**, *114*, 70–77.

[7] J. Lin, Z. Peng, Y. Liu, F. Ruiz-Zepeda, R. Ye, E. L. G. Samuel, M. J. Yacaman, B. I. Yakobson, J. M. Tour, "Laser-induced porous graphene films from commercial polymers" *Nat. Commun.* **2014**, *5*, 5714.

[8] J. Kotakoski, C. Brand, Y. Lilach, O. Cheshnovsky, C. Mangler, M. Arndt, J. C. Meyer, "Toward Two-Dimensional All-Carbon Heterostructures via Ion Beam Patterning of Single-Layer Graphene" *Nano Lett.* **2015**, *15*, 5944–5949.

[9] X. Wu, X. Luo, H. Cheng, R. Yang, X. Chen, "Recent progresses on ion beam irradiation induced structure and performance modulation of two-dimensional materials" *Nanoscale* **2023**, *15*, 8925–8947.

[10] G. Bräuchle, S. Richard-Schneider, D. Illig, J. Rockenberger, R. D. Beck, M. M. Kappes, "Etching nanometer sized holes of variable depth from carbon cluster impact induced defects on graphite surfaces" *Appl. Phys. Lett.* **1995**, *67*, 52–54.

[11] G. Bräuchle, S. Richard-Schneider, D. Illig, R. D. Beck, H. Schreiber, M. M. Kappes, "STM investigation of energetic carbon cluster ion penetration depth into HOPG" *Nuclear Instruments and Methods in Physics Research Section B: Beam Interactions with Materials and Atoms* **1996**, *112*, 105–108.

[12] Y.-J. Zhu, A. Schnieders, J. D. Alexander, T. P. Beebe, "Pit-Templated Synthesis and Oxygen Adsorption Properties of Gold Nanostructures on Highly Oriented Pyrolytic Graphite" *Langmuir* **2002**, *18*, 5728–5733.

View Article Online
DOI: 10.1039/D6NR00926C

[13] B. Prével, L. Bardotti, S. Fanget, A. Hannour, P. Mélinon, A. Perez, J. Gierak, G. Faini, E. Bourhis, D. Mailly, “Gold nanoparticle arrays on graphite surfaces” *Applied Surface Science* **2004**, *226*, 173–177.

[14] P. Mélinon, A. Hannour, L. Bardotti, B. Prével, J. Gierak, E. Bourhis, G. Faini, B. Canut, “Ion beam nanopatterning in graphite: characterization of single extended defects” *Nanotechnology* **2008**, *19*, 235305.

[15] A. Böttcher, M. Heil, N. Stürzl, S. S. Jester, S. Malik, F. Pérez-Willard, P. Brenner, D. Gerthsen, M. M. Kappes, “Nanostructuring the graphite basal plane by focused ion beam patterning and oxygen etching” *Nanotechnology* **2006**, *17*, 5889.

[16] A. Böttcher, D. Löffler, N. Bajales, S. Ulas, R. Machatschek, S. Malik, P. Brenner, M. M. Kappes, “Nanostructured arrays of stacked graphene sheets” *Nanotechnology* **2012**, *23*, 415302.

[17] A. Böttcher, R. Schwaiger, T. M. Pazdera, D. Exner, J. Hauns, D. Strelnikov, S. Lebedkin, R. Gröger, F. Esch, B. A. J. Lechner, M. M. Kappes, “Nanoscale patterning at the Si/SiO2/graphene interface by focused He+ beam” *Nanotechnology* **2020**, *31*, 505302.

[18] D. Löffler, S. Ulas, S.-S. Jester, P. Weis, A. Böttcher, M. M. Kappes, “Properties of non-IPR fullerene films versus size of the building blocks” *Phys. Chem. Chem. Phys.* **2010**, *12*, 10671–10684.

[19] S.-S. Jester, D. Löffler, P. Weis, A. Böttcher, M. M. Kappes, “Morphology of *C*n thin films ($50 \leqslant n < 60$) on graphite: Inference of energy dissipation during hyperthermal deposition” *Surface Science* **2009**, *603*, 1863–1872.

[20] P. Mélinon, A. Hannour, B. Prével, L. Bardotti, E. Bernstein, A. Perez, J. Gierak, E. Bourhis, D. Mailly, “Functionalizing surfaces with arrays of clusters: role of the defects” *Journal of Crystal Growth* **2005**, *275*, 317–324.

[21] H. Li, “Determination of oxygen functionality on Highly Oriented Pyrolytic Graphite (HOPG)” **2012**, DOI 10.17169/refubium-13709.

[22] D. Nečas, P. Klapetek, “Gwyddion: an open-source software for SPM data analysis” *Open Physics* **2012**, *10*, 181–188.

[23] M. Dienwiebel, G. S. Verhoeven, N. Pradeep, J. W. M. Frenken, J. A. Heimberg, H. W. Zandbergen, “Superlubricity of Graphite” *Phys. Rev. Lett.* **2004**, *92*, 126101.

[24] S. Ulas, S. Bundschuh, S.-S. Jester, C. Eberl, O. Kraft, H. Hölscher, A. Böttcher, M. M. Kappes, “Mechanical properties of C58 materials and their dependence on thermal treatment” *Carbon* **2014**, *68*, 125–137.

[25] D. Löffler, S.-S. Jester, P. Weis, A. Böttcher, M. M. Kappes, “Deuteration-induced scission of C58 oligomers” *J. Chem. Phys.* **2006**, *125*, 224705.

[26] T. Zecho, A. Güttler, X. Sha, B. Jackson, J. Küppers, “Adsorption of hydrogen and deuterium atoms on the (0001) graphite surface” *J. Chem. Phys.* **2002**, *117*, 8486–8492.

[27] T. Zecho, B. D. Brandner, J. Biener, J. Küppers, “Hydrogen-Induced Chemical Erosion of a-C:H Thin Films: Product Distribution and Temperature Dependence” *J. Phys. Chem. B* **2001**, *105*, 6194–6201.

[28] M. Komlenok, S. Tikhodeev, T. Weiss, S. Lebedev, G. Komandin, V. Konov, “All-carbon diamond/graphite metasurface: Experiment and modeling ” *Appl. Phys. Lett.* **2018,** *113,* 041101.

View Article Online
DOI: 10.1039/D6NR00926C

Data availability

The data presented in this manuscript are available upon request.